Journal of Marine Science and Application (2026) 25: 1176-1195
https://doi.org/10.1007/s11804-025-00738-w

RESEARCH ARTICLE

Effects of Intervening Water Layers on the Penetration Performance of Underwater Shaped Charge Jets

Minhui Gu[1], Kui Tang[1], Lingquan Kong[1], Jingwen Xia[1], Yangchen Gu[1], Yuanbo Li[1] and Jinxiang Wang[1]

Received: 30 April 2025 / Accepted: 26 June 2025
© Harbin Engineering University and Springer-Verlag GmbH Germany, part of Springer Nature 2026

Abstract

The penetration performance of an underwater shaped charge jet (USCJ) under the influence of an intervening water layer was studied by combining experimental and numerical simulation methods, considering the effects of initiation manners and standoff distance. First, the USCJ formation and its penetration performance tests were carried out, which were used to verify the reliability of the numerical simulation. Then, the formation and penetration processes of the shaped charge jet were analyzed experimentally and numerically. The results showed that during the penetration of the intervening water layer, the high-speed and high-energy jet head was engulfed by the water layer. A 30 mm intervening water layer reduces the kinetic energy of USCJ by approximately 13.6% and its penetration performance by 12.8%. The depth of penetration (DOP) of the USCJ decreases with increasing water layer thickness, and its decreasing trend gradually slows down. The DOPs of USCJ under annular and surface initiation manners are greater than those under central initiation. When the annular initiation radius increases, the accumulation effect of the USCJ weakens, and the overall velocity and kinetic energy increase, resulting in a significant increase in DOP. The DOP of USCJ increases initially and then decreases with an increase in the standoff distance; however, an increase in the water layer thickness reduces the optimal standoff distance. While the water layer reduces DOP, it also has a certain effect on the standoff distance. A certain thickness of the water layer is beneficial for the improvement of the DOP when the standoff distance is small.

Keywords Underwater shaped charge jet; Water layer; Initiation manner; Standoff distance; Penetration performance

1 Introduction

With the development of modern military technology, the destructive performance of weapon systems has received increasing attention. Shaped charge warheads, as an efficient means of destruction, are crucial for improving the destructive capabilities of underwater weapons. Currently, research on underwater shaped charge warheads primarily focuses on the behavior of metal jets in water and their destructive capabilities against underwater targets.

Since the 1980s, scholars have been conducting extensive research on the movement of shaped charge jets in water. High-speed photography and spectrometry techniques were used to investigate the behavior of metal jets in water. Fuhs et al. (2010) found that when a metal jet penetrates water, an irregularly shaped cavity forms behind it. Lee et al. (1995) used flash radiography and high-speed photography to study the penetration of particle-shaped jets into water and discovered that the morphology of the cavity is wavy. Held et al. (1987; 1990; 1995; 1996) employed the profile streak technique for the first time to measure the radial bubble growth process generated by jet penetration in water media. They studied the penetration processes of copper, aluminum, and tantalum jets in water and proposed the Szendrei–Held equation to describe the cavity formed by jets entering water, based on the Szendrei equation. Lam and Mcqueen (1998) carried out research on water penetration of explosively formed projectiles (EFPs) for mine disposal and found that EFPs lose their mine-clearing capability after penetrating water beyond two to three times the charge diameter. Wang et al. (2006) proposed a shaped charge with an eccentric subhemisphere liner and found that a "cavity-following effect" can be gen-

Article Highlights

- The high-velocity and high-energy jet head was engulfed by the water layer, significantly reducing the overall kinetic energy of the jet before it penetrates the target.
- A 30 mm intervening water layer reduces the kinetic energy of USCJ by approximately 13.6% and its penetration performance by 12.8%.
- The DOP of the USCJ on the No. 45 steel target decreases with increasing water layer thickness, and the decreasing trend gradually levels off.

✉ Kui Tang
tkui2014@sina.com

[1] National Key Laboratory of Transient Physics, Nanjing University of Science and Technology, Nanjing 210094, China

erated by appropriately selecting the charge length-to-diameter ratio and standoff distance. Zhang et al. (2010) experimentally compared the water penetration performance of tungsten–copper and copper liners under the same explosive-to-liner mass ratio and found that the velocity decay rate of the jet in water decreases with increasing material density. Wu et al. (2020) compared the formation processes of jets in air and water and discovered that the resistance and cooling effects of the water medium considerably affect the formation and elongation of metal jets. Chen and Lu (2024) investigated the factors influencing the underwater motion characteristics of jetting projectile charge (JPC). The results indicated that increasing the liner thickness, density, and charge length-to-diameter ratio can enhance the erosion resistance and velocity retention capabilities of JPCs. Ma et al. (2025) investigated the formation mechanism of cavities along with the evolution of their dimensions and geometries. The findings revealed that the expansion rates of the cavity length and maximum radius increase with jet impact kinetic energy.

Regarding the destructive capabilities of shaped charge jets against underwater targets, Cao and Liang (2001) theoretically, experimentally, and numerically studied the complete process of shaped charge jets penetrating water and metal targets. Yang et al. (2009) studied the penetration effects of EFPs against a water-containing composite armor and found that using a shaped charge with a variational-wall-thickness hemispherical liner is beneficial for penetrating large-gap water-containing composite armor protection structures. Shimamura and Ootsuka (2013) measured the pressure propagation and the elastic response of tank walls after shaped charge jets entered a large water tank. These data can be used to further analyze the hydrodynamic ram phenomenon. Hussain (2013) designed a copper liner to study its underwater penetration performance. The numerical and experimental results showed that the velocity of EFPs rapidly decreases in water, falling below the critical value after traveling five cone diameters, thus restricting it from penetrating a 5 mm-thick aluminum target. Zhang et al. (2017a; 2017b; 2020; 2022b) used an improved smoothed particle hydrodynamics method to study the damage effects of underwater shaped charge jets (USCJs) and explosive loads on plates, as well as the influence of three different liner shapes on the formation and penetration performance of USCJs. They also proposed a new annular-shaped charge structure, which demonstrated considerably better destructive effects than traditional-shaped charges. Wang et al. (2017) studied the behavior patterns of EFPs penetrating spaced targets underwater. Liu et al. (2020) numerically investigated the effects of different liquid tank parameters on the penetration performance and velocity attenuation of shaped charge jets. Gu et al. (2022; 2023) established a new theoretical model for the USCJ formation using the virtual mass method. Based on the theoretical model, they analyzed the effects of different factors on the formation characteristics and penetration capability of USCJs and a comparative study was carried out on USCJs and shaped charge jets in air. Zhang et al. (2024; 2025) investigated the damage characteristics of blasting, shaped, and linear-shaped charges on stiffened plates. The experimental results demonstrate that linear-shaped charges can create larger penetration holes on target plates, shaped charges exhibit stronger penetrating power, and blasting charges induce more significant deflection in the stiffened plates. Xu et al. (2023) studied the fundamental characteristics of underwater hypervelocity-shaped charges and shock waves. By comparing the diameter of cracks and residual velocities, they found that when the liner is made of aluminum, the metal jet exhibits the strongest penetration capability.

In summary, the unique properties of the water environment have a remarkable effect on the underwater motion characteristics and penetration performance of shaped charge jets. Based on the aforementioned published papers, current research primarily focuses on the formation of shaped charge jets in the air and on the subsequent underwater movement and destructive performance of these jets, while research on the formation of USCJs and their destructive performance is limited. When there is a gap between an underwater shaped charge warhead and the target, the influence of the intervening water on the penetration performance of the underwater-formed shaped charge jet remains unclear. Moreover, current research often emphasizes qualitative analysis of the jet formation process and penetration capability, lacking quantitative studies on influencing factors. To fill these research gaps, studies on the formation and penetration performance of a USCJ were carried out experimentally and numerically in the present paper. The effects of intervening water layer, initiation manner, and standoff distance on the penetration performance of USCJ were also analyzed, aiming to provide support for the design of underwater shaped charge munitions.

2 Penetration performance test

2.1 Experimental procedure

Figure 1 shows the static test device for underwater shaped charges. The device includes an underwater shaped charge warhead, a target, and a water tank. The shaped charge warhead was waterproofed in advance, and the water level was sufficient to submerge it. The shaped charge was detonated using a central initiation method during the experiment. In the first test, the warhead was attached to the target. In the second test, a nylon ring was placed between the front end of the warhead and the target, creating a 30 mm-thick water layer. In the two tests, the standoff distance S was 180 mm. The diameter and height of the booster, which

was made of phlegmatized RDX, were 14 and 6 mm, respectively. The main charge was made of 8701 explosive, with a diameter and height of 5 050 and 65 mm, respectively. The truncated conical liner was made of oxygen-free high-conductivity copper (Cu-OFHC), with a thickness of 2 mm, a diameter of 50 mm, and a cone angle of 60° . The target was made of No. 45 steel (a medium carbon high-strength steel widely used in China) and had a thickness of 180 mm.

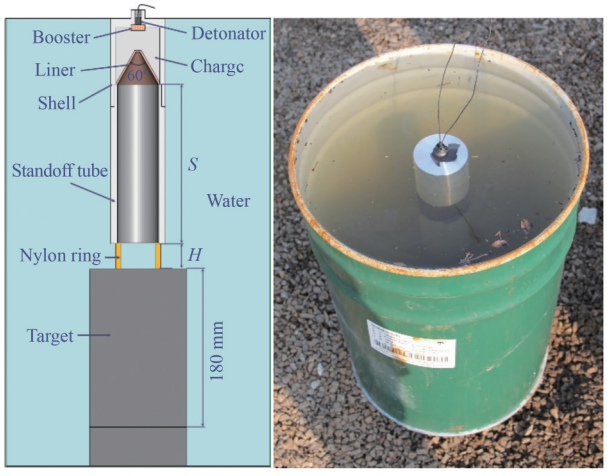


Figure 1 Diagram of the test device installation

2.2 Experimental results and discussion

To reveal the influence mechanism of the intervening water layer on the penetration performance of the USCJ, a test was conducted with a 30 mm water layer between the warhead and the target, which was compared with the condition where they are in direct contact. The depth of penetration (DOP) of the USCJ into the No. 45 steel target under the two conditions was obtained. After the test, the target was cut to expose the cross section, and the DOP was measured. The penetration data and target perforation morphology of the two tests are summarized in Table 1.

As shown in Table 1, Case 1 exhibits a porous metal layer attached to the near-wall surface of the jet penetration channel, which was formed by high-temperature molten metal jets adhering to the channel wall during penetration. The shapes of the penetration channels under the two conditions are similar, with a larger entrance diameter and a relatively constant diameter in the middle section. The overall diameter of the penetration channel is larger when the jet passes through the water layer before penetrating the target. This is likely due to the jet head deforming because of water resistance before coming into contact with the target. The DOP of the USCJ directly penetrating the No. 45 steel target is 149.3 mm. When there is a water layer with a thickness of 30 mm between the warhead and the target, the DOP decreases to 134.6 mm, which shows a reduction of 9.8% compared to Case 1.

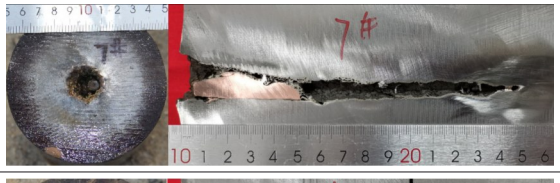
3 Numerical simulation

The experiment revealed that the presence of a water layer between the warhead and the target significantly affects the penetration performance of the USCJ on the No. 45 steel target. This study aims to understand how the water medium affects the formation and penetration performance of the USCJ. Numerical simulations will be used to further study the jet formation and its penetration performance under the influence of the water medium.

3.1 Numerical simulation model and algorithm

To obtain sufficient data to analyze the effect of the intervening water layer on the penetration performance of the USCJs, numerical simulations have been conducted. These simulations included different water layer thicknesses, initiation manners, and standoff distances. The structured arbitrary Lagrangian–Eulerian (S-ALE) algorithm was used for the calculations. In this model, air, water, explosives, and the liner are calculated using the Eulerian algorithm, with shared node processing between the grids. The shell, target, and water tank are calculated using the Lagrangian algorithm. The S-ALE algorithm is a second-order accurate advection algorithm based on the unified continuum

Table 1 Summary of the data of the warhead and target plate

Case	DOP (mm)	Water layer thickness (mm)	Section
1	149.3	0	
2	134.6	30	

theory momentum conservation equation, using a structured grid to discretize the fluid space. The contact algorithm obtains the interface force during the contact interaction between objects. This method effectively addresses issues of large spatial displacement and significant deformation of objects. The flow field control equations of the S-ALE algorithm consist of the mass, momentum, and energy conservation equations (Ma et al., 2024):

$$\frac{\partial \rho}{\partial t} = -\rho \frac{\partial v_i}{\partial x_i} - w_i \frac{\partial \rho}{\partial x_i} \tag{1}$$

$$\rho \frac{\partial v_i}{\partial t} = \frac{\partial \sigma_{ij}}{\partial x_j} + \rho b_i - \rho w_j \frac{\partial v_i}{\partial x_j} \tag{2}$$

$$\rho \frac{\partial E}{\partial t} = \sigma_{ij} v_{i,j} + \rho b_i v_i - \rho w_j \frac{\partial E}{\partial x_j} \tag{3}$$

where ρ is the fluid density; t is the time; v_i is the fluid velocity; w_i is the relative velocity between the material velocity and the reference coordinate, which is usually called the convection term; x_i is the Euler coordinate; σ_{ij} is the stress tensor; b_i is the body force per unit mass acting on a fluid element; E is the specific energy; and the subscripts i and j indicate grid coordinates. Common types of body forces include gravity, electromagnetic forces, and inertial forces arising in noninertial reference frames. In this study, the body force term b_i, representing external forces per unit mass such as gravity, is included in the governing equations. However, under the specific conditions of our simulations (characterized by short-duration high-intensity explosive events), these body forces are negligible compared to dominant forces like pressure gradients and stress divergences.

The effect of the fluid pressure gradient is not explicitly present in each equation, but it is indirectly incorporated through the stress tensor σ_{ij}. In practical applications, the stress tensor often contains a pressure term, especially for incompressible fluids, and it is given as

$$\sigma_{ij} = -p\delta_{ij} + \tau_{ij} \tag{4}$$

where p is the pressure, δ_{ij} is the Kronecker delta, and τ_{ij} is the viscous stress tensor. The term $-p\delta_{ij}$ represents the isotropic part of the Cauchy stress tensor, whose spatial divergence contributes to the pressure gradient force in the momentum equation.

The S-ALE algorithm is easier to achieve the structure–fluid boundary coupling and can effectively solve the leakage problem caused by the ALE penalty function coupling method. Additionally, the structured grid calculation converges more easily and requires less memory compared to the ALE solver (Qian et al., 2024).

Figure 2 shows the finite element model and boundary conditions of the USCJ penetrating the target plate. The numerical simulation setup in this study is consistent with the experimental conditions. A nonreflective boundary is applied to the outer air domain, and the constraint effect of the water tank on the water is simulated through a fluid–structure coupling method. Due to the geometric symmetry of the simulation model, this study establishes a three-dimensional 1/4 model for analysis based on the assumption of symmetry, and symmetric boundary conditions are applied on the symmetry planes. This approach reduces computational complexity and resource requirements without compromising the accuracy of the results. The Lagrange solver is employed for the target to improve the computational efficiency. Fixed boundary conditions are applied around the edges of the target to constrain its motion. Meanwhile, the target is discretized by a transition grid, and the jet penetration area is refined. The minimum size of the Euler and Lagrangian elements is 0.5 mm. The interaction between the jet and the target is achieved using a fluid–structure coupling method, which can effectively solve the problem of the interaction between compressible fluid and the rigid structure.

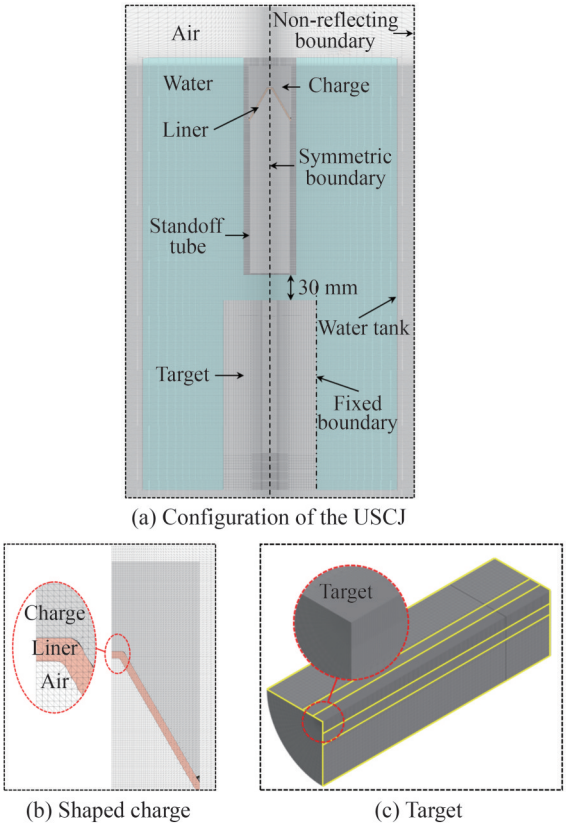


Figure 2 Finite element model and mesh division

3.2 Constitutive model and parameters

For penetration problems, the yield stress of metal materials is mainly influenced by strain hardening, strain rate, and temperature evolution. Thus, the Johnson–Cook and

Steinberg constitutive models, which are widely adopted in explosion and impact dynamic problems, were used in this study (Tang et al., 2022).

The liner, target, and shell are made of Cu-OFHC, No. 45 steel, and 6061 aluminum alloy, respectively. The materials of the target and shell are described by the Johnson–Cook strength–failure model and the Grüneisen equation of state (EOS). The expanded form of the Johnson–Cook stress–strain relationship is

$$\sigma = \left(A + B \cdot \bar{\varepsilon}^{n}\right)\left(1 + C\ln\dot{\varepsilon}^{*}\right)\left(1 - T^{*m}\right) \tag{5}$$

where $T^{*} = (T - T_r)/(T_m - T)$; T_m and T_r are the melting temperature and the room temperature, respectively; $\bar{\varepsilon}$ and $\dot{\varepsilon}$ are the effective plastic strain and the nondimensional plastic strain rate, respectively; and A, B, n, C, and m are material constants. Fracture in the Johnson–Cook material model is based on a cumulative damage law. When the effective cumulative plastic strain of the element reaches the failure strain, the element will erode. The failure mode is described as

$$D = \sum \frac{\Delta\bar{\varepsilon}}{\varepsilon_f} \tag{6}$$

in which

$$\varepsilon_f = \left[D_1 + D_2 \exp\left(D_3\sigma^{*}\right)\right]\left(1 + D_4 \ln\dot{\varepsilon}^{*}\right)\left(1 + D_5 T^{*}\right) \tag{7}$$

where $\Delta\bar{\varepsilon}$ is the increment of the effective plastic strain during an increment in loading, σ^{*} is the average stress normalized by the effective stress, and D_1–D_5 are fracture constants. Failure of the element is assumed to occur when $D = 1$. The failure strain ε_f and the accumulation of damage are functions of average stress, strain rate, and temperature. Numerical simulation will check the failure modes of materials at each time step to ensure accurate capture of the material failure process. During the computation, the damage variable of each element is continuously updated and examined at each incremental time step to determine whether it has reached the failure threshold. The parameters related to the Johnson–Cook model used in this study are shown in Table 2.

Due to the high temperature and high pressure of the detonation products, the liner is crushed rapidly to form a metal jet. The strain rate of the liner reaches 10^4–10^7 s^{-1}, and the maximum strain exceeds 10. Therefore, the Steinberg constitutive model is used to simulate liner deformation under extremely high strain rates ($> 10^5$ s^{-1}). The shear modulus G of the material before melting is defined as

$$G = G_0\left\{\begin{aligned}&1 + \left(G_p'/G_0\right)pV^{1/3} - \left(G_T'/G_0\right)\cdot\\&\left[\left(E - E_c\right)/3R' - 300\right]\end{aligned}\right\}e^{fE/(E_m - E)} \tag{8}$$

where the yield stress σ_Y is given by

$$\sigma_Y = \sigma_0\left[1 + \beta\left(\gamma_i + \bar{\varepsilon}\right)\right]^{n}\cdot \left\{\begin{aligned}&1 + \left(G_p'/G_0\right)pV^{1/3} -\\&\left(G_T'/G_0\right)\left[\left(E - E_c\right)/3R' - 300\right]\end{aligned}\right\}e^{fE/(E_m - E)} \tag{9}$$

where G_0 is the initial shear modulus; σ_0 and σ_m are the initial yield stress and the maximum yield stress, respectively; and V is the ratio of the current volume to the initial volume of the material. It is used to describe the effect of volume changes under high-pressure conditions on the yield stress. p is the pressure, γ_i is the initial plastic strain, $\bar{\varepsilon}$ is the effective plastic strain, β is a material constant, and f is a correction coefficient. G_p' and G_T' are the partial derivatives of the shear modulus versus pressure and temperature, respectively. E, E_c, and E_m are the internal energy, cold compression energy, and melting energy, respectively. E_c and E_m are given by

$$E_c(x) = \int_o^x p\mathrm{d}x - 900R'\exp(\alpha x)/(1 - x)^{2(\gamma_0 - \alpha - 1/2)},\quad x = 1 - V \tag{10}$$

$$E_m(x) = E_c(x) + 3R'T_m(x),\quad T_m(x) = T_{m0}\exp(2\alpha x)/V^{2(\gamma_0 - \alpha - 1/3)} \tag{11}$$

where R' is defined by $R' = R\rho/A_1$, with R being a gas constant, ρ being the density, and A_1 being the atomic weight. T_m is the melting temperature, T_{m0} is the melting temperature at normal pressure, γ_0 is the Grüneisen constant, and α is a correction constant. When the material melts, G and σ_Y are set to one-half their initial values (Tang et al., 2023). The parameters related to the Steinberg model used in this study are shown in Table 3.

Table 2 Johnson–Cook model parameters of the shell and target (Holmquist et al., 2001; Li et al., 2023; Bardiani et al., 2025)

Material	ρ (g/cm^3)	A (MPa)	B (MPa)	n	C	m	D_1	D_2	D_3	D_4	D_5
6061-Al	2.704	324	114	0.42	0.002	1.34	−0.77	1.45	−0.47	0.000	1.60
No. 45 steel	7.800	507	320	0.28	0.064	1.06	0.10	0.76	1.58	0.005	−0.84

Table 3 Steinberg model parameters of the liner (Steinberg et al., 1980)

ρ (g/cm^3)	G_0 (GPa)	σ_0 (GPa)	σ_m (GPa)	β	n
8.93	47.7	0.12	0.64	36	0.45
G_p'/G_0 (TPa^{-1})	G_T'/G_0 (kK^{-1})	T_{m0} (K)	γ_0	α	
28	0.38	1 790	2.02	1.5	

The charge uses 8701 explosive, and the pressure of the detonation products of the high-energy explosives is usually described by the Jones–Wilkins–Lee (JWL) EOS. The JWL EOS is a function of pressure p, relative volume V, and initial specific internal energy E_0, and its general form is

$$p = C_1\left(1 - \frac{\omega}{R_1 V}\right)\mathrm{e}^{-R_1 V} + C_2\left(1 - \frac{\omega}{R_2 V}\right)\mathrm{e}^{-R_2 V} + \frac{\omega E_0}{V} \quad (12)$$

where ω, C_1, C_2, R_1, and R_2 are material constants obtained through experiments. The JWL material parameters of the 8701 explosive are shown in Table 4.

Table 4 Explosive material parameters (Liu, 2006)

ρ (g/cm^3)	D_v (m/s)	ω	C_1 (GPa)
1.787	8 390	0.35	581.4
C_2 (GPa)	R_1	R_2	E_0 (GPa)
6.8	4.1	1.0	9

During the process of an underwater explosion, water exhibits obvious compressibility. To better reflect the compression and expansion processes of water, the Mie–Grüneisen EOS is used to describe these processes, and its general form is

$$p = \frac{\rho_0 C^2 \mu\left[1 + \left(1 - \frac{\gamma_0}{2}\right)\mu - \frac{a}{2}\mu^2\right]}{\left[1 - (S_1 - 1)\mu - (S_2 - 1)\frac{\mu^2}{\mu + 1} - S_3\frac{\mu^3}{(\mu + 1)^2}\right]^2} \quad (13)$$

For expanding materials,

$$p = \rho_0 C^2 \mu + (\gamma_0 + a\mu)E \quad (14)$$

where C is the velocity of sound in water; S_1, S_2, and S_3 are dimensionless coefficients obtained from experimental fitting; γ_0 is the Grüneisen constant; α is the correction factor for γ_0; μ is the compression ratio; and E is the initial specific internal energy. The material parameters of water are shown in Table 5.

Table 5 EOS parameters of water (Guo et al., 2019)

ρ_0 (g/cm^3)	C (m/s)	γ_0	α	S_1	S_2	S_3	E (MPa)
1.0	1 480	0.28	0	1.75	0	0	0

For air, a linear polynomial EOS is used to describe its physical state:

$$p = C_0 + C_1\mu + C_2\mu^2 + C_3\mu^3 + \left(C_4\mu + C_5\mu + C_6\mu^2\right)E \quad (15)$$

where C_i represents the EOS parameters, μ is the compression ratio, and E is the initial specific internal energy. Air is considered an ideal gas, and its material parameters are shown in Table 6.

Table 6 EOS parameters of air (Zhang et al., 2022a)

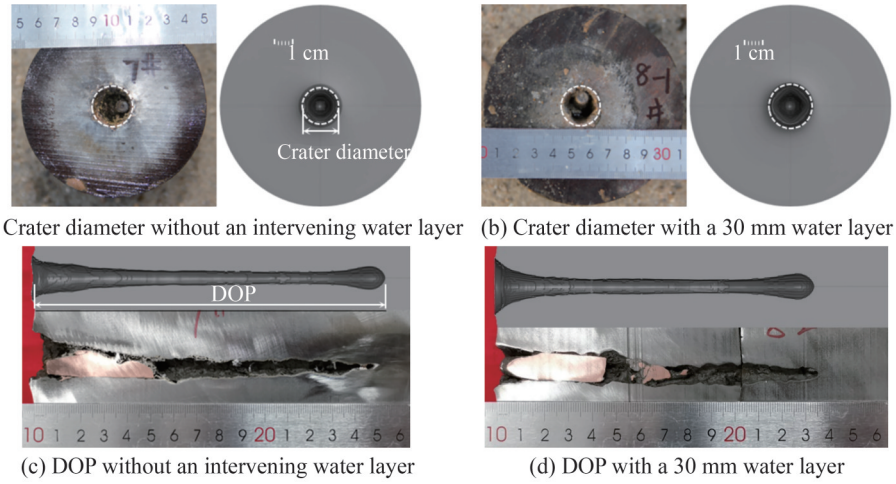
ρ_0 (kg/m^3)	C_0	C_1	C_2	C_3	C_4	C_5	C_6	E (MPa)
1.29	0	0	0	0	0.4	0.4	0	0.25

3.3 Numerical simulation validity verification

The results of two USCJ penetration tests are presented in Section 2. To verify the reliability of the numerical simulation model and material parameters, the test conditions were reproduced, and the experimental values of DOP and crater diameter were used as validation criteria. Figure 3 and Table 7 present the penetration results from both the experiments and numerical simulations under two different conditions. As shown in Figure 3 and Table 7, the numerical results are in good agreement with the experimental data, including the penetration channel morphology, DOP, and crater diameter. Under both conditions, the error in the DOP between the simulation and experiment is within 2.4%.

In addition, to verify the mesh sensitivity of the numerical simulation model, the condition with a 30 mm water layer was used as an example. Ensuring the mesh ratio between the Euler and Lagrange refinement zones was 1∶1, the minimum grid sizes are set as 0.4, 0.5, 0.6, 0.8, and 1.0 mm for the simulation. The DOP for different mesh sizes is shown in Figure 4. The number of mesh elements for the fluid and solid corresponding to different mesh sizes is shown in Table 8. As shown in Figure 4 and Table 8, when the minimum grid size is less than 0.5 mm, the simulation results agree well with the experimental results, with an error of less than 1%. Considering both computational efficiency and simulation accuracy, the minimum mesh size of the following models was set to 0.5 mm.

In conclusion, the material parameters and numerical simulation model used in this study are reliable and can accurately simulate the formation and the penetration process of the USCJ into the No. 45 steel target. Further numerical simulation research can be conducted on this basis.



(a) Crater diameter without an intervening water layer (b) Crater diameter with a 30 mm water layer

(c) DOP without an intervening water layer (d) DOP with a 30 mm water layer

Figure 3 Comparison between numerical and experimental results

Table 7 DOP of the USCJ at different water layer thicknesses

Case	Water layer thickness (mm)	Experimental DOP (mm)	Simulated DOP (mm)	Error (%)	Experimental crater diameter (mm)	Simulated crater diameter (mm)	Error (%)
1	0	149.3	152.9	2.4	22.1	19.9	9.9
2	30	134.6	133.4	0.9	21.6	23.2	7.4

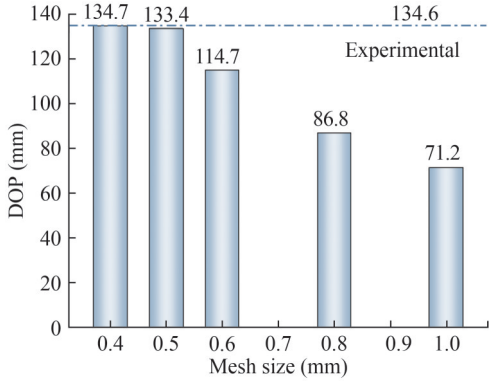


Figure 4 DOP for different mesh sizes

Table 8 Total number of mesh elements corresponding to different mesh sizes

Mesh size (mm)	Number of fluid mesh elements	Number of solid mesh elements	Number of mesh elements
0.4	7 162 608	717 043	7 879 651
0.5	5 003 811	541 531	5 545 342
0.6	3 386 564	452 883	3 839 447
0.8	1 724 463	382 531	2 106 994
1.0	1 337 500	361 351	1 698 851

4 Results and discussion

4.1 Analysis of the USCJ formation and penetration processes

4.1.1 Jet formation process

In this section, numerical simulations based on the two test conditions are carried out, focusing on the analysis of the formation process of the USCJ. Figure 5 shows the propagation of the detonation wave during the formation of the USCJ and the shaped charge jet in air. From the result at 4 μs in Figure 5, under central initiation, the detonation wave of the USCJ propagates to the liner in the form of a spherical wave. The liner collapses under the action of the detonation wave and begins to converge toward the center, with the maximum detonation pressure at the wavefront reaching 26.4 GPa. When a wave propagates from a high-impedance material to a low-impedance material, the reflected wave appears as a rarefaction wave, which rapidly reduces the pressure in the originally compressed region (Li et al., 2019). As shown in the result at 4 μs in Figure 5(a), after the detonation wave reaches the shell and the liner, due to the impedance mismatch, part of the detonation wave transmits into the shell and liner, while another part is reflected, as indicated by regions A_2 and A_3 in the figure. At this moment, the shock wave transmitted into the shell reflects at the shell–water interface and forms a rarefaction wave, causing fragmentation of the shell, as seen in region A_1. By approximately 5.6 μs, a distinct low-pressure region can be observed behind the reflected shock wave from the liner, as indicated in region B_3. This is because the liner has a higher wave impedance, and the shock wave transmitted back into the detonation products from the liner creates a low-pressure zone. Similarly, the low-pressure region at B_1 is caused by transmission from the shell. At this point, the shock wave has already transmitted into the water, as indicated in region B_2. The propagation of the detonation wave during the formation of the shaped charge jets in air is shown in Figure 5(b). Unlike the

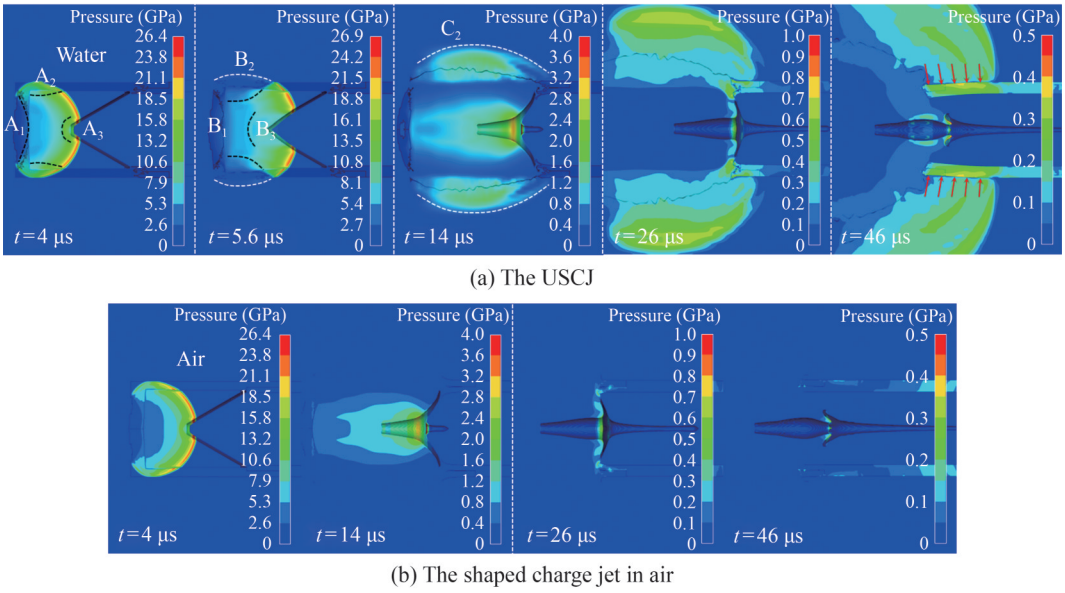


Figure 5 Propagation of the detonation wave during the formation

shaped charge acting in air, from 4 to 14 μs, the diffusion of detonation products is limited by the combined effect of the water and shell, reducing the loss of detonation energy. At 26 μs, the jet is basically formed. Because the medium inside the standoff tube under the liner is air, its wave impedance is much smaller than that of the liner material, so the intensity of the shock wave transmitted to the front air is very small. However, due to the high wave impedance of the water medium, the intensity of the shock wave transmitted into the water remains high enough, and the transmitted shock wave attenuates slowly in water. As shown in the result at 14 μs in Figure 5(a), the shock wave transmitted into the water in region C_2 forms a distinct high-pressure zone near the shell. The pressure difference between inside and outside the standoff tube causes the part of it near the charge to collapse and converge toward its axis. At approximately 46 μs, the pressure difference between inside and outside the standoff tube reaches up to 0.2 GPa, and an obvious shrinkage behavior is presented on the standoff tube. Additionally, the jet is about to perforate the standoff tube. In contrast, as shown in the result at 46 μs in Figure 5(b), the shock wave transmitted into the surrounding air is negligible, and the standoff tube does not exhibit a shrinkage behavior. As shown by the area marked with red arrows in Figure 5(a), the diameter of the shrunken standoff tube is still larger than the diameter of the jet tail and the slug, so it does not affect the formation of the jet. In addition, the jet is already fully formed before the shock wave reflected from the water tank wall propagates to the central axis, so it also does not affect the formation of the USCJ. Furthermore, the explosive pressure of the charge is much greater than the hydrostatic pressure in the test and simulation conditions, so it is believed that the shallow water environment does not affect the jet formation.

In the underwater test, the same shrinkage phenomenon was observed on the recovered standoff tube. As shown in Figure 6, measurement points are arranged at 15 mm intervals along the axial direction of the standoff tube. The radial deformation was recorded by measuring the outer diameter of the standoff tube at each measurement point. The final deformation results are listed in Table 9. According to Figure 6 and Table 9, the pressure difference between inside and outside the standoff tube caused by the shock wave transmitted into the water leads to radial compression deformation of the standoff tube. The closer the standoff tube is to the charge, the greater the shock wave pressure difference, so the shrinkage phenomenon at measurement points 7–10 is particularly obvious. For example, in the test, the outer diameter of the standoff tube at measurement point 10 is approximately 57.4 mm, which is reduced by 7.5% compared to the undeformed state. As the shock wave in the water continues to propagate, the pressure gradually attenuates, reducing the pressure difference between inside and outside the standoff tube, and the deformation of the standoff tube decreases correspondingly. By the time it reaches measurement point 5, the outer diameter of the standoff tube is approximately 61.3 mm, which is only 1.1% lower than the undeformed state. Furthermore, comparing the measured diameters of the standoff tube at each measurement point, the error between the simulation and the test results is less than 3%, which also further verifies the reliability of the simulation model.

Figure 7 shows the formation process of the USCJ corresponding to Case 2. As shown in Figure 7, during the jet formation stage, with the initiation of the explosive, the liner converges toward its central axis under the action of the shock wave and the detonation products at a high temperature and a high pressure, forming an initial jet at about

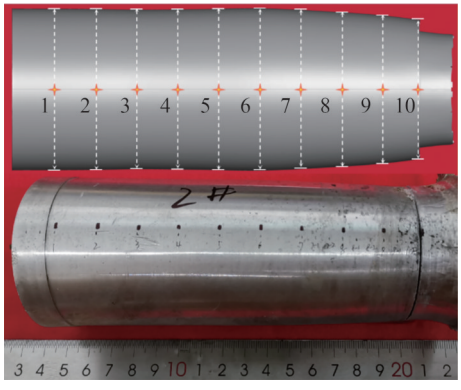


Figure 6 Comparison of the standoff tubes in the simulation and experiment

Table 9 Diameter data at various sections of the standoff tubes in the simulation and experiment

Measurementpoint	Experimental (mm)	Numerical (mm)	Error (%)
1	61.8	62.4	0.9
2	61.7	62.2	0.9
3	61.6	61.7	0.2
4	61.4	61.8	0.7
5	61.3	62.2	1.5
6	60.8	62.6	2.9
7	60.5	62.2	2.8
8	59.8	60.6	1.2
9	58.8	58.7	−0.2
10	57.4	55.8	−2.7

8 μs, with a velocity up to 5 524 m/s. From 8 to 18 μs, the detonation products continue to act on the liner, causing further collapse, resulting in a significant velocity difference between the front and rear ends of the jet. At 18 μs, the velocity difference reaches 5 040 m/s. After 18 μs, the liner is elongated under the influence of the velocity gradient. At about 26 μs, the jet is basically formed, with a head velocity of 5 351 m/s. At 46 μs, before the USCJ comes into contact with the bottom of the standoff tube, it is clearly divided into two parts: the slug and the jet, with a jet head velocity of 5276 m/s.

Additionally, in the results of 26–46 μs, it can be clearly observed that the jet head has a larger diameter, while before 18 μs, the diameter of the jet along the axis remains basically unchanged. This is due to the accumulation effect of the jet. As shown by the dashed line in the 8 μs results, the microelement at the tip of the liner does not reach the maximum collapse velocity when it reaches the axis, resulting in a relatively low jet head velocity (Shi et al., 2022). The maximum collapse velocity of the microelement of the liner appears near point *A* in the 12 μs result, reaching 5 804 m/s. This pushes the microelements converging at the axis before 12 μs (on the right of point *A*) forward, ultimately causing an accumulation phenomenon at the front of the jet, forming a jet head with a larger diameter.

4.1.2 Jet penetration process

When a water layer is present, the jet will penetrate the water and the No. 45 steel target in order. Therefore, the jet penetration process can be divided into penetrating the water layer and penetrating the No. 45 steel target. Figure 8 shows the process of the USCJ penetrating the water layer. As shown in Figure 8, at 47 μs, the jet comes into contact with the 30 mm-thick water layer, entering the water penetration stage, which lasts for about 8 μs. During the penetration process, the resistance of the water, which is much greater than that of the air, causes the jet head to deform. At 50 μs, it can be observed that the jet head, under the resistance of the water, takes on a distinct "mushroom head" shape. From 50 to 54 μs, as the jet continues to penetrate the water layer, the contact area between the jet head and the water further increases. From the dashed box of the 52 μs result, the outer metal jet flips backward under the action of resistance. At about 54 μs, a ring detached from the main body of the jet. Clearly, due to the presence of the 30 mm-thick water layer, the jet section with the highest velocity is almost completely engulfed by the water layer.

Additionally, before the jet penetrates the target, the water medium is impacted by the jet and forms a local high-pressure area near the contact surface, as shown in Figure 9. Pushed by the jet, the water medium first acts on the target. The response of the target before jet penetration is shown in Figure 10, where Figure 10(a) shows the sectional view and Figure 10(b) shows the top view. From Figures 9

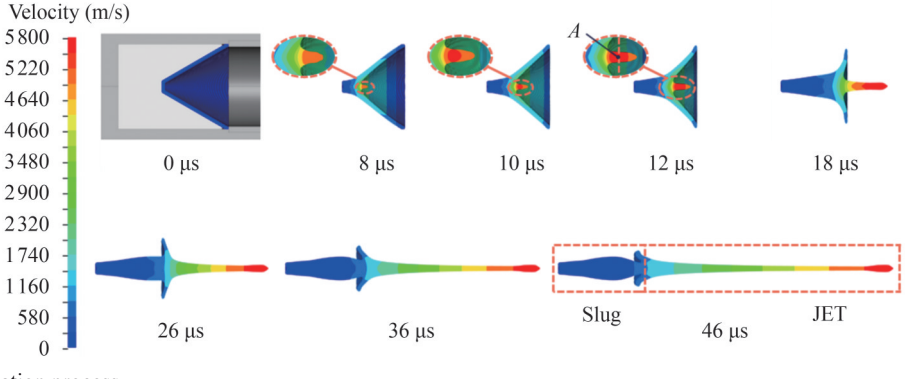


Figure 7 USCJ formation process

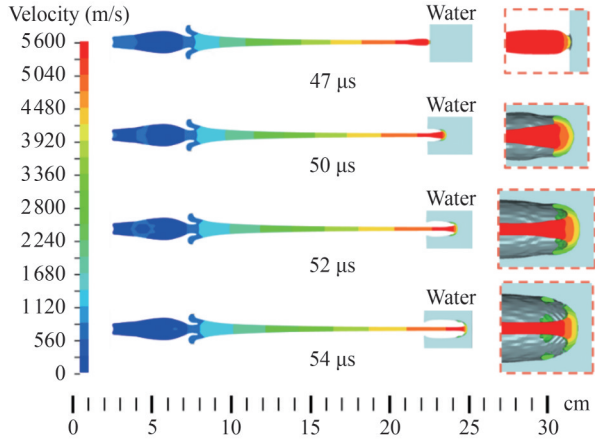


Figure 8 Process of USCJ penetration into the water layer

and 10, when there is a 30 mm water layer, although the jet has not yet touched the target, there is already a large stress in front of the target due to the action of the water. This phenomenon is known as the hydrodynamic ram effect (Guo et al., 2020). This stress is concentrated in the center of the target, radiating outward while gradually attenuating. Later, due to the failure of the center grid of the target under distortion, the stress began to decrease. Under the effect of the hydrodynamic ram effect, the target undergoes plastic deformation, forming an initial dent with a diameter up to 18.2 mm.

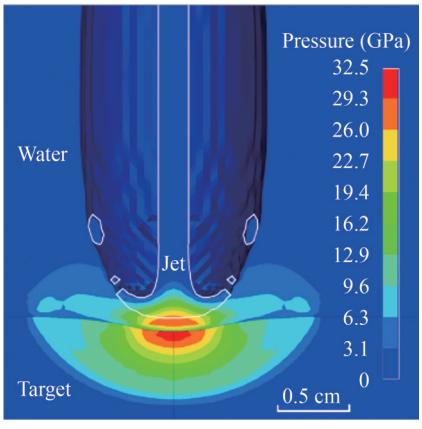


Figure 9 Local pressure contour before the jet penetrates the target with a 30 mm water layer

Under the condition without a water layer, the local pressure and stress cloud diagram before the jet penetrates the target are shown in Figures 11 and 12, respectively. From Figures 11 and 12, without the water layer, the jet acts directly on the target after formation, without penetrating the water medium. The wave impedance of air is pretty low, so the local high-pressure area formed ahead of the jet–air contact surface has a very low pressure. The stress generated before the jet penetrates the target is minimal and cannot cause plastic deformation of the target. Additionally, the detonation products cause the target to be subjected to the force transmitted by the standoff tube, forming an annular high-pressure area near the front surface. However, the stress is still insufficient to cause plastic deformation of the target.

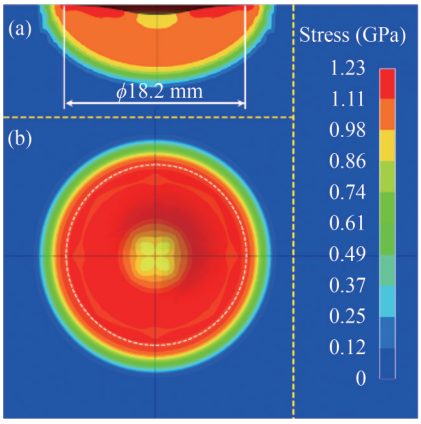


Figure 10 Local stress contour of the target before jet penetration with a 30 mm water layer

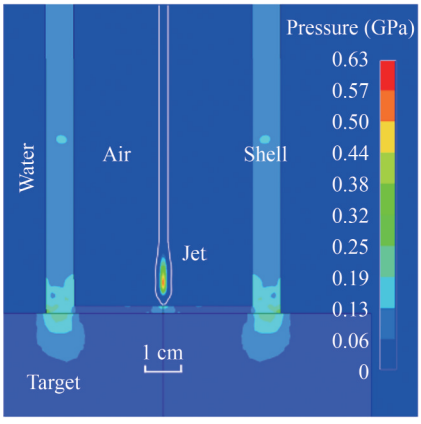


Figure 11 Local pressure contour before the jet penetrates the target without a water layer

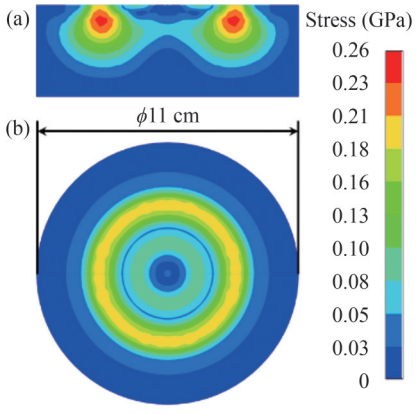


Figure 12 Local stress contour of the target before jet penetration without a water layer

The kinetic energy variation and DOP–time curves of the jet throughout the formation and penetration process

under the two simulation conditions are shown in Figure 13, which describes the stages of the USCJ penetrating the No. 45 steel target. Figures 14 and 15 show the penetration process of the USCJ under the two conditions. The analysis in this section is conducted in stages to facilitate horizontal comparison. From Figure 13, at 450 μs, the kinetic energy of the jet is completely consumed, indicating that 0–450 μs encompasses the entire process of USCJ formation and its penetration into the No. 45 steel target. Under the action of the shock wave and the detonation product, the kinetic energy of the liner quickly reaches its peak value, which is up to 88.1 kJ. Subsequently, the jet continues to move forward inside the standoff tube. During this process, as the standoff tube is filled with air, the kinetic energy of the jet decreases slightly due to air resistance. At 46 μs (as shown in Figure 14(a)), under the condition without water layer interference, the jet begins to penetrate the target. Because the wave impedance of the target is much higher than that of water, the kinetic energy of the jet decreases rapidly. From 46 to 150 μs, the jet is in a stable penetration stage, and the DOP increases almost linearly. Under the condition with a 30 mm water layer, the jet begins to penetrate the target at approximately 56 μs (as shown in Figure 15(a)). During this process, the water layer consumes about 12 kJ of the kinetic energy of the jet. From 56 to 150 μs, the jet is in a stable penetration stage, and the DOP increases rapidly.

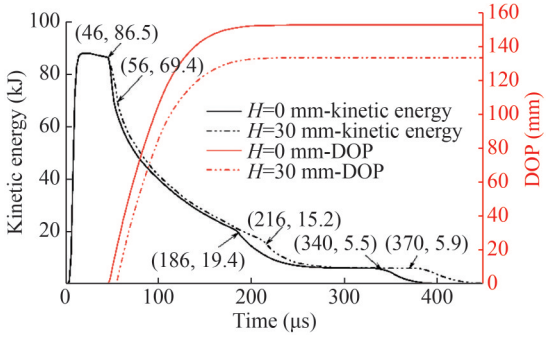


Figure 13 Time-history curves of jet kinetic energy and DOP

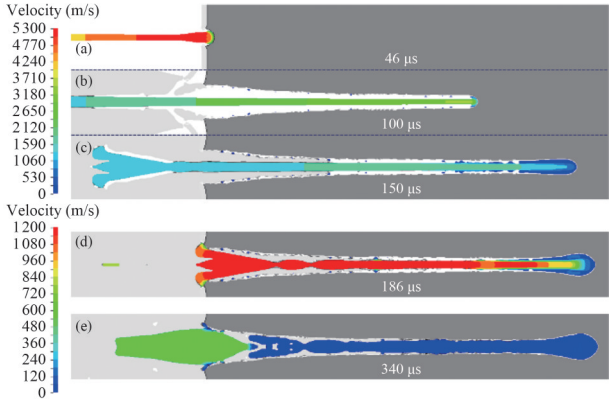


Figure 14 USCJ penetration process without a water layer

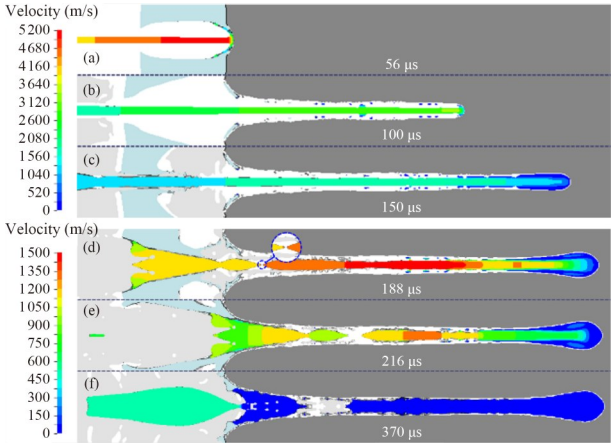


Figure 15 USCJ penetration process with a 30 mm water layer

As the penetration continues, the kinetic energy of the jet continuously decreases. As shown in the enlarged area in Figure 15(d), the jet begins to fracture at 188 μs. The rear part of the fractured jet comes into contact with the target at 216 μs and consumes part of the kinetic energy of the jet while enlarging the penetration hole in the target. At 370 μs, the slug comes into contact with the jet that previously penetrated the target, as shown in Figure 15(f). This results in a second penetration hole enlargement in the target until the kinetic energy of the jet is consumed completely. Therefore, as shown in Figure 13, under the condition with a 30 mm water layer, the kinetic energy curve shows inflection points at 216 and 370 μs. As shown in Figures 14(d) and (e), under the condition without a water layer, the jet also undergoes two hole enlargement stages at 186 and 340 μs during the penetration phase, leading to the accelerated consumption of the kinetic energy of the jet. In addition, when there is no water layer interference, the jet does not fracture during penetration. The action of the jet energy is more concentrated, and the kinetic energy used to penetrate the target is greater, resulting in a 12.8% larger DOP compared to the condition with a 30 mm water layer. Because the subsequent USCJ can only cause penetration hole enlargement, the DOP remains basically unchanged after 200 μs under the two conditions.

The velocity distribution of the USCJ was calculated using the virtual mass method proposed (Gu et al., 2022). This method considers the surrounding water medium as a virtual shell, assuming that during the explosion, the momentum and energy of the virtual shell are equal to those transferred into the water by the shock wave. It also assumes that the virtual shell and the charge casing have the same velocity. By applying the principles of momentum conservation and energy conservation, the mass of the virtual shell is determined, and the collapse velocity of the liner is then calculated using the Gurney equation for asymmetric sandwich structures. Figure 16 shows the velocity distribution and jet morphology obtained through theoretical calculation and numerical simulation just before the jets are in

contact with the No. 45 steel targets. As shown in Figure 16, the error between the jet velocity from the numerical simulation and the theoretical calculation curve is less than 5%, which once again proves the reliability of the numerical simulation. In the theoretical calculation, the PER theory considers the velocity to be decreased monotonically, resulting in the theoretical value of the jet head velocity being slightly higher than the simulation value. When there is a 30 mm water layer, the jet action time is longer, and the jet length is correspondingly longer due to the influence of the velocity gradient. Under the condition without a water layer, the jet head length generated by the accumulation effect can reach up to 15 mm. However, under the condition with a 30 mm water layer, the jet head is almost engulfed by the water layer due to the obstruction of the water layer, and the tip velocity of the jet decreases to 3 635 m/s. Moreover, comparing the kinetic energy of the USCJ just before penetrating the target under the two conditions shown in Figure 13 reveals a reduction of 12 kJ due to the 30 mm-thick water layer. This represents a decrease of about 14% in kinetic energy compared to the condition without a water layer. Ultimately, this leads to a significant reduction in the DOP with the 30 mm water layer.

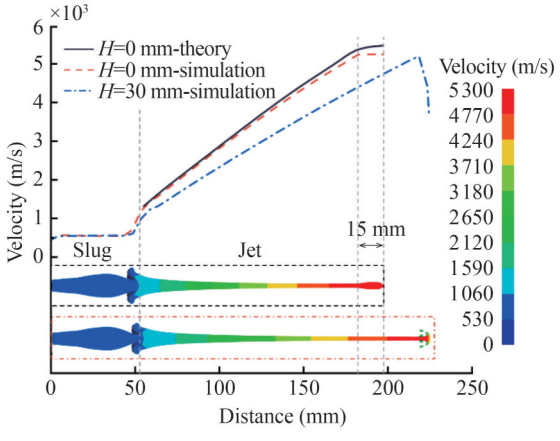


Figure 16 Velocity field and centerline velocity magnitude of the jet under two conditions

4.2 Analysis of the penetration performance of the USCJ

4.2.1 Influence of water layer thickness

Based on the above two test conditions, further analysis was carried out, with the added water layer thickness ranging from 50 to 300 mm in increments of 25 mm. The DOP results under different water layer thicknesses are shown in Figure 17, along with the fitting curve obtained by fitting the numerical simulation data. Figure 18 shows the proportion of jet kinetic energy consumed by the water and the target under different water layer thicknesses. The kinetic energy of the jet before coming into contact with the water is 86.5 kJ for each condition.

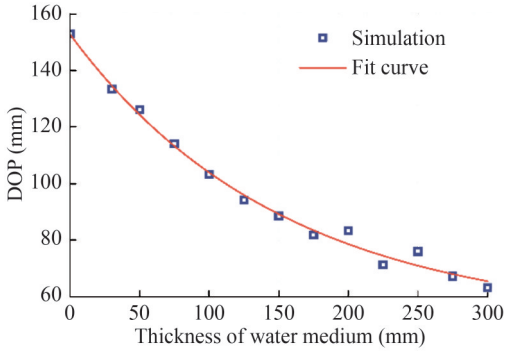


Figure 17 Relationship between DOP in the target and water layer thickness

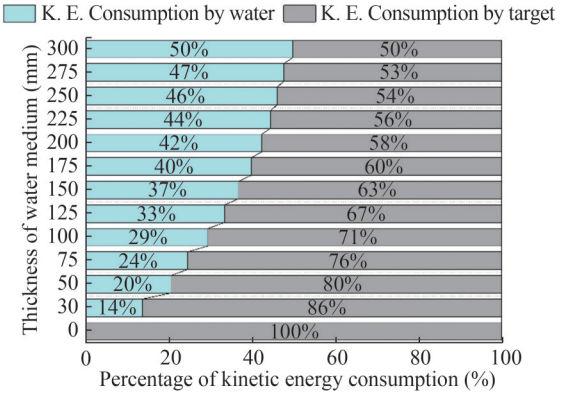


Figure 18 Proportion of the jet kinetic energy consumed by the water and target under different water layer thicknesses

From Figures 17 and 18, the DOP of the USCJ penetrating the No. 45 steel target decreases with increasing water layer thickness, and its decreasing trend gradually levels off. When the water layer thickness is 300 mm, the proportion of jet kinetic energy consumed by water reaches 50%. This is because as the water layer thickness increases, the kinetic energy of the jet consumed in the process of penetrating the water layer increases, resulting in the corresponding decrease in the DOP in the target. At the initial stage of the jet penetration into the water layer, its velocity is at its maximum, and the jet experiences greater penetration resistance, resulting in a higher kinetic energy consumption rate during the penetration. With the increase in DOP, both the jet velocity and the penetration resistance gradually decrease. Overall, as the water layer thickness increases, the attenuation rate of the jet velocity gradually decreases, and the resistance experienced in the water correspondingly decreases. The overall kinetic energy attenuation rate of the jet decreases, and the decreasing trend of the DOP correspondingly slows down.

To more intuitively display the motion and energy consumption of the USCJ in water, it is assumed that the jet penetrates an infinite water domain. The jet morphology and velocity cloud diagram at typical moments are shown in Figure 19. As shown in Figure 19, after the jet enters the water, the water medium is impacted to form a cavity that

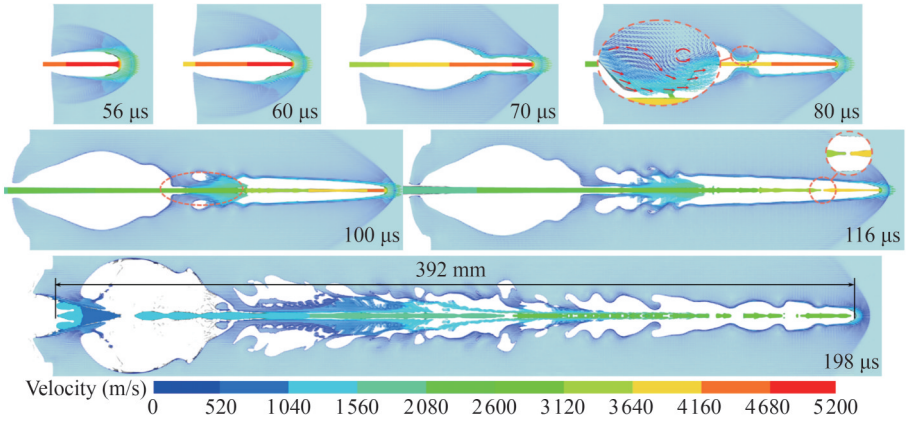


Figure 19 Movement process of the USCJ in the water medium

envelops the jet. At 56 μs, the cavity shape begins to change under the interference of collapsing jet fragments. At the interaction position between the jet and the cavity boundary, the water medium has velocity components consistent with the jet motion direction and significant radial velocity components. The velocity component along the jet penetration direction causes the cavity to continuously expand along the penetration direction, while the radial velocity component causes the cavity diameter to increase continuously. Although the velocity of the water medium at the cavity interface near the free surface has significantly decreased, there is still a considerable residual velocity. Therefore, the cavity does not immediately close under gravity but closes around 116 μs. By around 60 μs, the cavity shape near the jet head has significantly changed due to the influence of the detached jet fragments. Between 60 and 80 μs, the water medium flows toward the jet axis due to the interference of the detached jet fragments. By 80 μs, the middle section of the cavity closes and begins to make contact with the jet. The local enlarged view at 80 μs clearly shows the flow direction of the water medium. After 80 μs, due to the high velocity of the jet, the pressure near the jet within the cavity decreases according to Bernoulli's principle. The water medium, after coming into contact with the jet, is adsorbed around the jet under the pressure difference and moves forward with the jet. At 100 μs, as shown in the dashed box in the figure, the water medium adsorbed around the jet increases gradually, causing the jet in contact with water to tend to fracture. At 116 μs, the jet head is fractured due to the velocity gradient, and a significant amount of water medium is adsorbed around the jet in the middle section of the cavity. The pressure cloud diagram of the fluid near the penetration channel at this time is shown in Figure 20. As shown in Figure 20, the pressure along the jet axis within the cavity is lower than that outside. From Figure 19, at 198 μs, during the process of penetrating the water medium, the jet undergoes multiple fractures, forming several independent jet segments, and the cavity outline shows significant discontinuity. In contrast, the cavity profile obtained from the simulation in Ma et al. (2025) appears relatively smooth. Analysis shows that the above phenomena are caused by two factors. One is the adsorption effect of the jet, causing the water medium to flow toward the jet axis. Another is the penetration of the water medium by the jet segments ahead, causing the water medium to expand radially to form cavities, while shock waves form ahead of the cavities under the jet penetration. This penetration process is inherited by the next fractured jet segment, and the jet continues to penetrate the target until all segments are depleted. Due to the different velocities and lengths of the jet segments, the cavity outline is not a smooth curve but rather wavy, which is consistent with the phenomena observed in the experiments described in Fuhs et al. (2010). In addition, the relevant study in Ma et al. (2025) indicates that the cavity formed by a jet in water exhibits a conical shape. As shown in Figure 20, the cavity profile generated by the jet penetration also displays a conical distribution over a larger timescale. This phenomenon is primarily attributed to the velocity gradient within the jet, where the jet tip possesses the highest velocity and imparts greater radial momentum to the water during penetration. However, as the penetration continues, the high-velocity front segment of the jet is gradually depleted, and the velocity of the trailing jet decreases. Consequently, the radial velocity transferred to the surrounding water diminishes, ultimately resulting in a progressively narrower cavity diameter.

To further reveal the influence of the water layer, the ideal condition of forming in water and then flying freely in air was selected for simulation. The result at the moment of jet fracture is shown in Figure 21. As shown in Figure 21, the jet begins to fracture at 198 μs, with a maximum stretch length of 738 mm (excluding the slug). In contrast, the jet moving into the water has already broken into multiple segments under the interference of the surrounding water medium (see Figure 19 for the result at 198 μs), with a remaining jet length (excluding the slug) of only 392 mm, which significantly affects the penetration performance of the shaped charge jet.

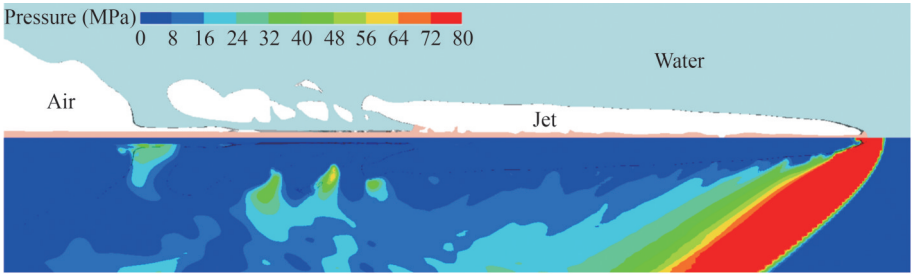


Figure 20 Fluid pressure contour in the penetration area at 116 μs

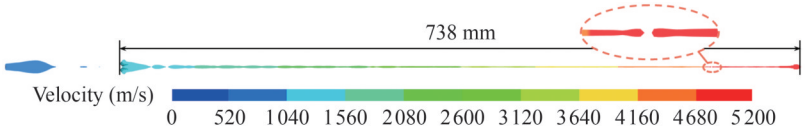


Figure 21 Shape of the USCJ at the moment of fracture during free stretching in the air

4.2.2 Influence of initiation manner

On the basis of revealing the mechanism of the USCJ penetrating the No. 45 steel target, the influence of the initiation manner will be analyzed here according to numerical simulation. The numerical simulation model setting is the same as that given in Figure 2, and both the initiation manner and the water layer thickness are changed. New initiation manners, such as annular initiation and surface initiation, are added, and water layer thicknesses of 0, 30, and 100 mm are considered.

Figure 22 shows the DOP results under different initiation manners and water layer thicknesses. The horizontal axis labels r = 5 mm, r = 15 mm, and r = 25 mm represent annular initiation with radii of 5, 15, and 25 mm, respectively. As shown in Figure 22, the jet DOPs under annular and surface initiation are larger than those under central initiation. When the annular initiation radius is the same as the charge radius (r = 25 mm), USCJ achieves the maximum DOP. Without water layer interference, the jet can completely perforate the front target with a thickness of 180 mm and penetrate the backward target. The effect of initiation manner on the DOP is consistent across different water layer thicknesses. To reveal the mechanism, the following is interpreted in terms of detonation waveforms and jet formation states.

Figure 23 shows the pressure contour diagrams of the detonation wave propagation under different initiation

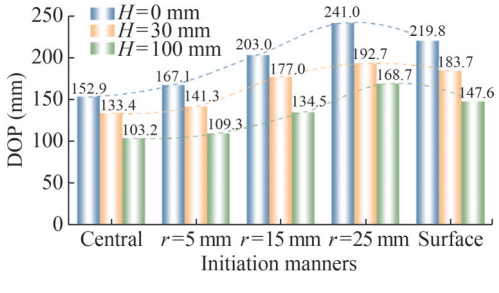


Figure 22 Depth of jet penetration into the target under different initiation manners and water layer thicknesses

manners. As shown in Figure 23(a), when the charge is initiated at the central point, the detonation wave propagates spherically toward the liner. When the wave reaches the middle section of the liner, the detonation wave propagation direction is nearly parallel to the liner generatrix (the angle between the normal of the detonation wavefront and the liner generatrix $\alpha = 2°$). At this moment, the pressure of the detonation wave is 24.7 GPa. Therefore, the collapse velocity of the liner and the DOP of the jet are also lower than those of the other initiation manners. When annular initiation is used (see Figures 23(b)–(d)), the detonation wave collides with the charge axis and forms a W shape as it propagates to the liner. The overlap pressures after detonation wave collisions are 31.7, 58.7, and 92.3 GPa for annular initiation radii of 5, 15, and 25 mm, respectively. Annular initiation causes regular oblique reflection or Mach reflection of the detonation wave on the central axis, resulting in a significant increase in the pressure in the overlap zone. As the annular initiation radius increases, the detonation wave gradually approaches a conical shape. When it propagates to the middle section of the liner, the angle α between the detonation wave propagation direction and the liner generatrix increases from 13° to 37°. The increase in detonation pressure is also significant, with the detonation pressures reaching 27.4, 33.6, and 39.1 GPa at the middle section of the liner, resulting in a corresponding increase in the jet velocity. When the initiation radius is 25 mm (see Figure 23(d)), α is approximately 37°, which is much larger than those of the other initiation manners, and the corresponding detonation pressure action on the liner is the highest. Therefore, the detonation energy acts more efficiently on the liner, facilitating the generation of jets with higher velocities. When surface initiation is used, the detonation wave propagates to the liner in the form of a plane wave, forming a surface high-pressure zone at the wavefront. When the shock wave propagates to the middle section of the liner, the detonation wave pressure is 37.7 GPa, and the propagation direction is parallel to the

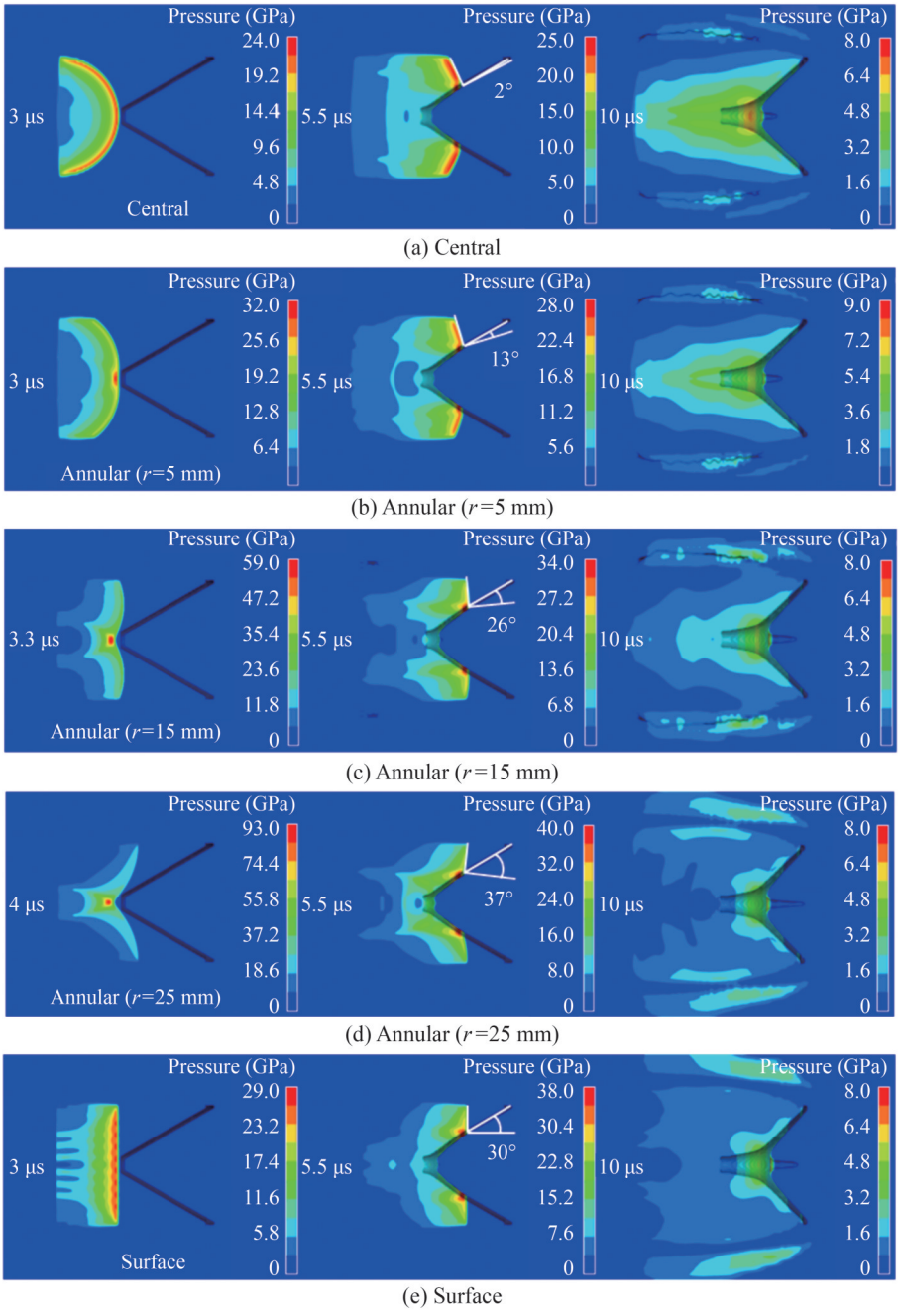


Figure 23 Pressure contour of the detonation wave propagation under different initiation manners

charge axis, with α of 30°. This value is only slightly lower than that under the condition with a 25 mm annular initiation radius and is consistent with the DOP variation across different initiation manners.

Figures 24 and 25 present the velocity distribution curves and the velocity cloud diagrams of the jet before perforating the standoff tube under different initiation manners, respectively. As shown in Figures 24 and 25, when the charge is initiated at the center (see Figure 25(a)), the velocity of the jet along its axis is lower than that of the other initiation manners. The accumulation effect of the jet head is the most evident in this case, with the jet head length reaching up to 15 mm, and the corresponding DOP is the smallest. When annular initiation is used and its radius increases gradually (see Figures 25(b)–(d)), the jet velocity increases correspondingly. When the annular initiation radius is 25 mm (see Figure 25(d)), the accumulation effect of the jet is the weakest, the jet head length is only 7 mm, and the jet head velocity is the highest, reaching up to 6 922 m/s, with the corresponding DOP being the largest. Compared with central initiation, the detonation waves formed under annular and surface initiation are more conducive to the liner collapsing toward its center. Due to the wave shape and the overlap pressure of the shock wave, less jet accu-

mulates at the head of the jet, and the overall velocity of the jet is higher, which ultimately leads to an increase in the DOP. Moreover, as shown in the dashed box in Figure 25, the slug formed under central initiation is the longest. When the annular initiation radius increases from 5 to 25 mm, the length of the slug decreases gradually. The length of the slug in the case of surface initiation is also less than that under central initiation, and that in the case of annular initiation with a radius of 25 mm is the shortest. This indicates that when using annular or surface initiation, more of the liner mass forms an effective jet for subsequent penetration, which is more beneficial for increasing the DOP.

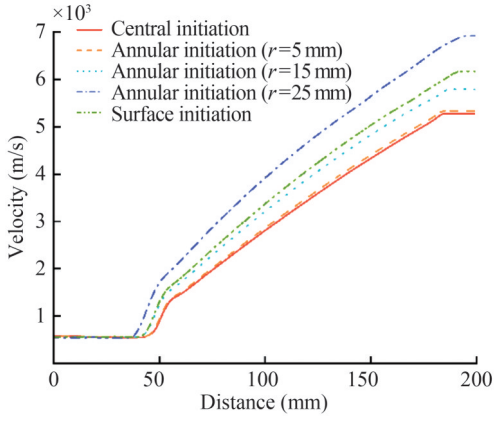


Figure 24 Velocity distribution curves of the jet under different initiation manners

Figure 26 shows the time-history curves of the jet kinetic energy under the interference of the 30 and 100 mm water layers with different initiation manners. Table 10 summarizes the kinetic energy of the jet before entering the water and before penetrating the target under different water layer thicknesses and initiation manners. From Figure 26 and Table 10, the differences in the detonation wave effects under different initiation manners lead to variations in the velocity and kinetic energy of the jet and in the time before the jet enters the water and comes into contact with the target. When annular initiation with a radius of 25 mm is used, the variation in the kinetic energy of the jet during

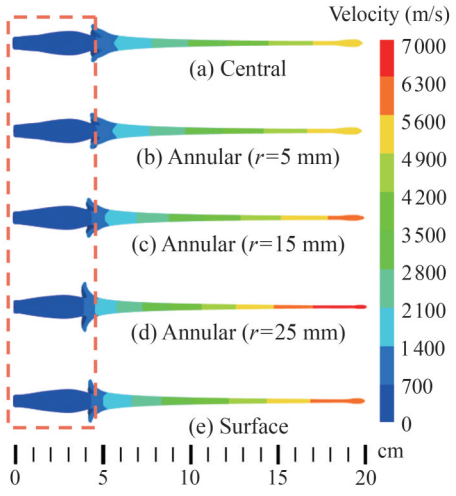
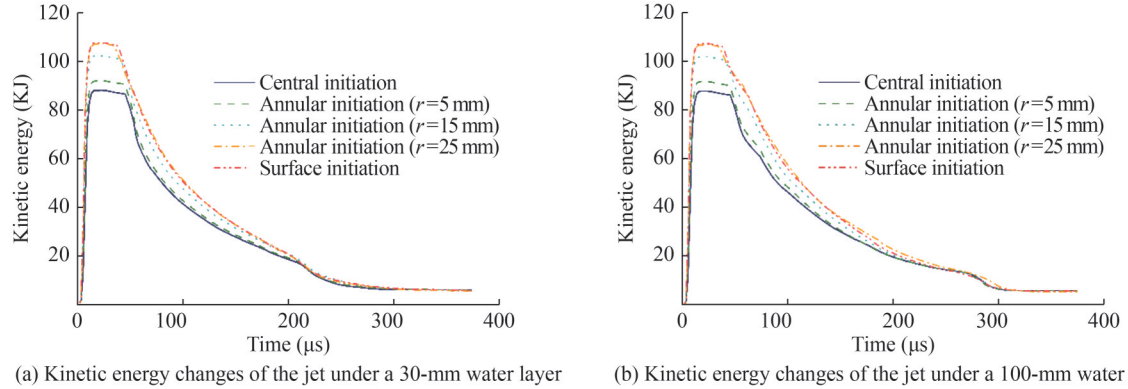


Figure 25 Velocity contour of the jet under different initiation manners

penetration is similar to that of surface initiation, with the jet kinetic energy before entering the water being around 106.5 kJ. The jet formed under central initiation has the fastest kinetic energy consumption rate during penetration of the water layer. According to Figures 7 and 25, this is due to the jet formation state. The jet formed under central initiation has the largest head diameter, increasing the contact area with water, resulting in greater penetration resistance. Even after the jet head is engulfed by the water layer, the jet diameter is still larger than those of the other initiation manners when the water layer is sufficiently thick to engulf the jet head.

During penetration of the water layer, the jet kinetic energy consumption rate is the fastest under central initiation, followed by annular initiation with a radius of 5 mm, whereas that under annular initiation with a radius of 25 mm is the slowest.

Figures 27 and 28 show the velocity distribution of the jet before it penetrates the target under the interference of the 30 and 100 mm water layers with different initiation manners, respectively. From Figures 27 and 28, the jet formed under central initiation creates the largest cavity in the water medium due to its slower velocity, allowing more



(a) Kinetic energy changes of the jet under a 30-mm water layer

(b) Kinetic energy changes of the jet under a 100-mm water layer

Figure 26 Time-history curves of jet kinetic energy under different initiation manners and water layer thicknesses

Table 10 Kinetic energy of the jet at typical moments under different water layer thicknesses and initiation manners

Initiation manner	Water layer thickness (mm)					
	0		30		100	
	Time of target contact (μs)	Kinetic energy at target contact (kJ)	Time of target contact (μs)	Kinetic energy at target contact (kJ)	Time of target contact (μs)	Kinetic energy at target contact (kJ)
Central	46.3	86.5	54.9	72.1	74.9	60.6
Annular (r = 5 mm)	45.3	90.5	53.7	77.0	73.4	64.2
Annular (r = 15 mm)	41.3	100.9	49.0	91.0	67.1	77.9
Annular (r = 25 mm)	35.4	106.5	42.1	100.3	58.5	90.2
Surface	39.2	106.5	46.5	96.9	64.2	85.3

time for the water to flow outward. As the annular initiation radius increases, the cavity volume decreases gradually. In addition, by comparing Figures 28(a) and (d), it can be clearly observed that the middle part of the cavity formed under central initiation is closed (as explained in detail in Section 4.1.2), creating two cavities, while the cavity formed under annular initiation with a radius of 25 mm is relatively complete. This is because the jet formed under central initiation has a larger jet head, resulting in a more pronounced collapse effect of the jet, which affects the flow of the water. Annular initiation effectively reduces the accumulation effect of the jet, and when the annular initiation radius is 25 mm, the accumulation effect is almost negligible, resulting in a relatively complete penetration cavity.

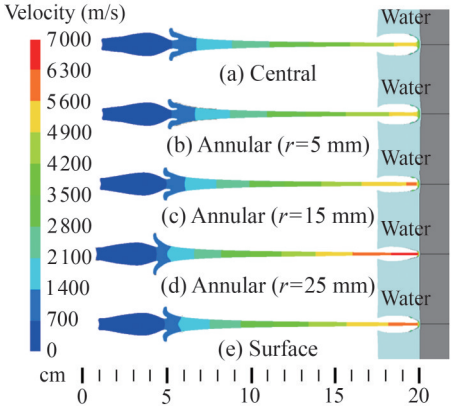


Figure 27 Velocity distribution of the jet before penetrating the target with a 30 mm water layer

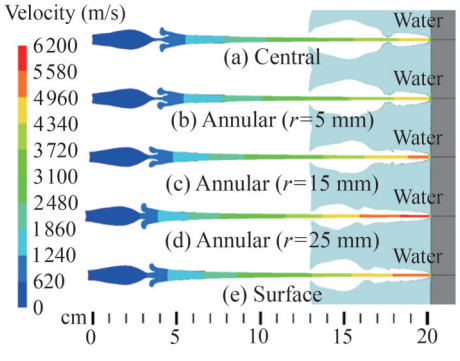


Figure 28 Velocity distribution of the jet before penetrating the target with a 100 mm water layer

Figure 29 shows the time-history curves of the DOP under the interference of the 30 and 100 mm water layers with different initiation manners. From Figure 30, the DOP reaches its maximum value at about 200 μs under different initiation manners. At this time, although the jet still has some kinetic energy, due to the front part of the jet cannot be ejected from the penetration channel, causing a blockage. On this basis, the subsequent jet loses its penetration ability, as shown by the velocity distribution and morphology of the jet in Figure 30, with the left side showing the condition with a 30 mm water layer and the right side showing the condition with a 100 mm water layer.

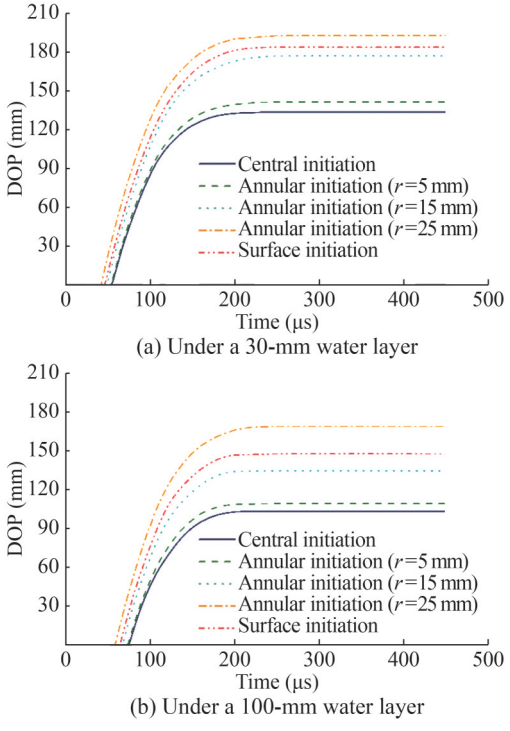


Figure 29 Time-history curves of DOP with different initiation manners and water layer thicknesses

4.2.3 Influence of standoff distance

On the basis of the above research, the effect of standoff distance on the DOP under different water layer thicknesses is further discussed in this section, as shown in Figure 31.

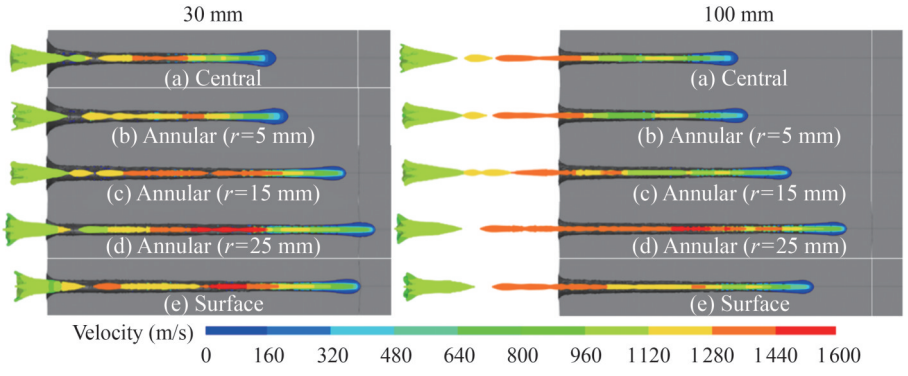


Figure 30 Velocity distribution and perforation condition after DOP stabilization

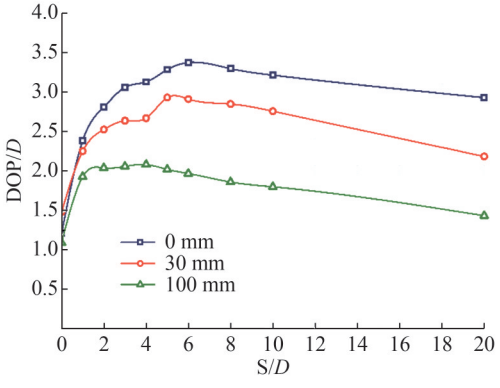


Figure 31 Variation curves of the DOP with standoff distance for different water layer thicknesses

In Figure 31, *S*/*D* is the ratio of the standoff distance to the charge diameter, and DOP/*D* is the ratio of the DOP to the charge diameter. From Figure 31, similar to the shaped charge jet in the air, the USCJ also has an optimal standoff distance when penetrating the target. As the standoff distance increases, the DOP of the USCJ first increases and then decreases. Due to the velocity gradient of the jet, it will gradually elongate in the action process. A jet with appropriate length can enhance the penetration performance, but when the jet elongates to a certain length, necking and fracture occur, resulting in reduce of the penetration performance. Before reaching the optimal standoff distance, an increase in the standoff distance causes a rapid increase in the DOP, while the DOP decreases slowly after the standoff distance exceeds the optimal one. An increase in the water layer thickness reduces the optimal standoff distance. Without water layer interference, the optimal standoff distance for the jet is about six times the charge diameter. With 30 and 100 mm water layers, the optimal standoff distance is approximately five and four times the charge diameter, respectively. This is because the wave impedance difference between the water and the target is significant. To some extent, the water layer acts as part of the standoff distance, which reduces the optimal standoff distance. Additionally, when the *S*/*D* is 0, the DOP under the condition with a 30 mm water layer is greater than that without water layer interference. This further indicates that while the water layer reduces the DOP, it also has a certain effect on the standoff distance. A certain thickness of the water layer is beneficial for increasing the DOP when the standoff distance is small.

5 Conclusions

A combined experimental and numerical simulation investigation on the penetration performance of a 50 mm caliber USCJ under the influence of an intervening water layer, as well as the influence of the initiation manner and the standoff distance, is considered. The main conclusions are as follows:

1) During penetration of the water layer by USCJ, the jet head gradually forms a "mushroom head," and then the ring is detached from the main body of the jet. The high-velocity, high-energy jet head is engulfed by the water layer, considerably reducing the overall kinetic energy of the jet before it penetrates the target. A 30 mm-thick water layer consumes about 14% of the kinetic energy of the jet, resulting in a 12.8% decrease in its DOP.

2) The DOP of USCJ on the No. 45 steel target decreases with increasing water layer thickness, and its decreasing trend gradually levels off. When the water layer reaches 300 mm, the water medium engulfs the high-velocity high-energy front section of the jet and adsorbs the water to move toward the jet axis during penetration. This results in premature jet breakup, leading to a final DOP of only 63.2 mm—representing a 58.7% reduction compared with the condition without water layer interference.

3) During the formation of USCJ, there is an accumulation phenomenon at the front end of the jet, forming a larger diameter jet head. Under the condition without a water layer, the jet head length can reach up to 15 mm. When the shaped charge jet is formed underwater, the shock wave propagating through the shell into the water attenuates slowly, resulting in a substantial shrinkage near the front end of the

standoff tube.

4) The effect of the initiation manners on the DOP is consistent across different water layer thicknesses. The DOPs of the jet under annular and surface initiation are greater than those in the case of central initiation. As the radius of the annular initiator increases, the detonation pressure on the liner increases, and the angle α between the detonation wave propagation direction and the liner generatrix increases from 13° to 37°. The accumulation effect of the USCJ weakens, and the overall jet velocity and the DOP increase. During penetration of the water layer, the jet kinetic energy consumption rate follows the order central initiation > annular initiation with a radius of 5 mm > annular initiation with a radius of 15 mm > annular initiation with a radius of 25 mm ≈ surface initiation.

5) For different water layer thicknesses, the DOP of the USCJ first increases and then decreases with increasing standoff distance. However, increasing the water layer thickness reduces the optimal standoff distance. The water layer acts as part of the standoff distance, which reduces the optimal standoff distance and the DOP. A 30 mm-thick water layer is beneficial for increasing the DOP when S/D is less than 0.6.

Acknowledgement This research was funded by National Natural Science foundation of China (Nos. 12372361), and the Fundamental Research Funds for the Central Universities (No. 30924010833).

Competing interests The authors have no competing interests to declare that are relevant to the content of this article.

References

Bardiani J, Lomazzi L, Sbarufatti C, Manes A (2025) A machine learning-based tool to correlate coupled and uncoupled numerical simulations for submerged plates subjected to underwater explosions. Journal of Marine Science and Application. https://doi.org/10.1007/s11804-025-00624-5

Cao JZ, Liang LH (2001) Demonstration of numerically simulating figures for underwater explosions. Proceedings of the 24th International Congress on High-Speed Photography and Photonics, Sendai, Japan, 4183. https://doi.org/10.1117/12.424347

Chen X, Lu YG (2024) Research on the influences of motion characteristics of jetting projectile charge under water. Defence Technology 33: 411-425. https://doi.org/10.1016/j.dt.2023.07.009

Fuhs AE, Buck JA, Hallenbeck AE, Strott JB (2010) Metal combustion in steam. Naval Engineers Journal 97(3): 65-79. https://doi.org/10.1111/j.1559-3584.1985.tb01322.x

Gu YC, Wang JX, Li H, Liu LT, Tang K, Ma T, Lin SJ (2023) Comparative study on the forming characteristics and penetration effects of shaped charge jet in water and air. Journal of Applied Physics 133(11): 115901. https://doi.org/10.1063/5.0139683

Gu YC, Wang JX, Li H, Tang K, Liu LT (2022) Formation characteristics and penetration performance of an underwater shaped charge jet. Ocean Engineering 258: 111695. https://doi.org/10.1016/j.oceaneng.2022.111695

Guo M, Zu XD, Shen XJ, Huang ZX (2019) Study on liquid-filled structure target with shaped charge vertical penetration. Defence Technology 15(6): 861-867. https://doi.org/10.1016/j.dt.2019.05.003

Guo ZT, Chen T, Mu ZC, Zhang W (2020) An investigation into container constraint effects on the cavity characteristics due to high-speed projectile water entry. Ocean Engineering 210: 107449. https://doi.org/10.1016/j.oceaneng.2020.107449

Held M (1987) Refined shaped charge jet penetration measurement in various materials. Proceedings of 10th International Symposium on Ballistics, 1-8

Held M (1995) Verification of the equation for radial crater growth by shaped charge jet penetration. International Journal of Impact Engineering 17(1-3): 387-398. https://doi.org/10.1016/0734-743X(95)99864-N

Held M, Backofen JE (1990) Penetration of shaped charge into water. 12th International Symposium on Ballistics, San Antonio, 30-40

Held M, Huang NS, Jiang D, Chang CC (1996) Determination of the crater radius as a function of time of a shaped charge jet that penetrates water. Propellants Explosives Pyrotechnics 21(2): 64-69. https://doi.org/10.1002/prep.19960210203

Holmquist TJ, Templeton DW, Bishnoi KD (2001) Constitutive modeling of aluminum nitride for large strain, high-strain rate, and high-pressure applications. International Journal of Impact Engineering 25(3): 211-231. https://doi.org/10.1016/S0734-743X(00)00046-4

Hussain G, Hameed A, Hetherington JG, Malik AQ, Sanaullah K (2013) The explosively formed projectile (EFP) as a standoff sea mine neutralization device. Journal of Energetic Materials 31(2): 100-114. https://doi.org/10.1080/07370652.2011.587862

Lam C, Mcqueen D (1998) Study of the penetration of water by an explosively formed projectile. Defence Science and Technology Organization 21: 19

Lee ES, Oh KH, Song SY (1995) Penetration of particulated shaped-charge jet into water. 21st International Congress on High-Speed Photography & Photonics, 975-981. https://doi.org/10.1117/12.209556

Li L, Han B, He SY, Zhao ZY, Zhang R, Zhang QC, Lu TJ (2019) Shock loading simulation using density-graded metallic foam projectiles. Materials & Design 164: 107546. https://doi.org/10.1016/j.matdes.2018.107546

Li YB, Wang JX, Liu ZT, Tang K, Wang HF, Chen XW (2023) Orthogonal optimization design and experiments on explosively formed projectiles with fins. International Journal of Impact Engineering 173: 104462. https://doi.org/10.1016/j.ijimpeng.2022.104462

Liu F (2006) The explosively formed penetrator and its engineering damage effects research. PhD thesis, University of Science and Technology of China, Hefei. (in Chinese)

Liu NN, Ren SF, Song DD, Liu LT (2020) Damage research of shaped charge jet on warship broadside. Journal of Ship Mechanics 24(8): 1072-1080. (in Chinese) https://doi.org/10.3969/j.issn.1007-7294.2020.08.012

Ma SX, Li XD, Zhou LW (2025) Experimental and numerical investigation of cavity characteristics in behind-armor liquid-filled containers under shaped charge jet impact. Defence Technology 47: 242-259. https://doi.org/10.1016/j.dt.2024.12.021

Ma T, Wang JX, Liu LT, Li H, Tang K, Gu YC, Zhang YF (2024) Study on structural response of water-back plate under the combined action of shock wave and bubble loads generated by cylindrical charge in deep-water environment. Thin-Walled Structures 194: 111307. https://doi.org/10.1016/j.tws.2023.111307

Qian ZH, Yang TM, Liu MB (2024) An overview of coupled Lagrangian–Eulerian methods for ocean engineering. Journal of Marine Science and Application 23: 366-397. https://doi.org/10.1007/s11804-024-00404-7

Shi J, Huang ZX, Zu XD, Xiao QQ (2022) Experimental and numerical investigation of jet performance based on Johnson-Cook model of liner material. International Journal of Impact Engineering 170: 104343. https://doi.org/10.1016/j. ijimpeng.2022.104343

Shimamura K, Ootsuka T (2013) Study of water entry of high-speed projectile. Procedia Engineering 58: 232-239. https://doi.org/10.1016/j.proeng.2013.05.027

Steinberg DJ, Cochran SG, Guinan MW (1980) A constitutive model for metals applicable at high-strain rate. Journal of Applied Physics 51(3): 1498-1504. https://doi.org/10.1063/1.327799

Tang K, Wang JX, Liu LT, Yang M (2023) Study on the mechanism of secondary penetration of long rod and its influencing factors. Acta Armamentarii 44(12): 3707-3718. (in Chinese) DOI: 10.12382/bgxb.2023.0035

Tang K, Wang JX, Song HP, Zhou N (2022) Investigation on the penetration of jacketed rods with striking velocities of 0.9–3.3 km/s into semi-infinite targets. Defence Technology 18(3): 476-489. https://doi.org/10.1016/j.dt.2021.03.003

Wang HF, Jiang ZR, Yu WM, Liu ZW (2006) Behavior of jetting penetrator charge operating underwater. Transactions of Beijing Institute of Technology 26(3): 189-192. (in Chinese) https://doi.org/10.15918/j.tbit1001-0645.2006.03.001

Wang YJ, Li WB, Wang XM, Li WB (2017) Numerical simulation and experimental study on flight characteristics and penetration against spaced targets of EFP in water. Chinese Journal of Energetic Materials 25(6): 459-465. (in Chinese) DOI: 10.3969/10.11943/j.issn.1006-9941.2017.06.003

Wu JY, Zhong MS, Liu Y, Xie XB, Ji C (2020) Study on the influencing factors of underwater unexploded ordnance destruction based on shaped charged jet. Journal of Physics: Conference Series 1507(3): 032007. https://doi.org/10.1088/1742-6596/1507/3/032007

Xu LY, Tian Y, Liu XB, Wang SP (2023) Numerical investigation on jet penetration capacity of hypervelocity shaped charge in underwater explosion. Ocean Engineering 281: 114668. https://doi.org/10.1016/j.oceaneng.2023.114668

Yang L, Zhang QM, Ju YY (2009) Experimental study on the penetration of explosively formed projectile against water-partitioned armor. Transactions of Beijing Institute of Technology 29(3): 197-200. (in Chinese) https://doi.org/10.15918/j.tbit1001-0645.2009.03.007

Zhang XR, Wu C, Huang FL (2010) Penetration of shaped charge jets with tungsten–copper and copper liners at the same explosive-to-liner mass ratio into water. Shock Waves 20(3): 263-267. https://doi.org/10.1007/s00193-010-0248-0

Zhang YF, Liu LT, Wang JX, Tang K, Ma T (2022a) Study on the impact characteristics of underwater explosion bubble jets induced by plate structure. Ocean Engineering 266: 112641. https://doi.org/10.1016/j.oceaneng.2022.112641

Zhang ZF, Li HL, Zhang JY, Wang LK, Zhang GY, Zong Z (2024) Characterization of underwater explosive loads of blasting and shaped charges. Journal of Marine Science and Application 23(2): 302-315. https://doi.org/10.1007/s11804-024-00422-5

Zhang ZF, Wang C, Xu WL, Hu HL (2020) Penetration of annular and general jets into underwater plates. Computational Particle Mechanics 8(2): 289-296. https://doi.org/10.1007/s40571-020-00330-9

Zhang ZF, Wang C, Xu WL, Hu HL, Guo YC (2022b) Application of a new type of annular shaped charge in penetration into underwater double-hull structure. International Journal of Impact Engineering 159: 104057. https://doi.org/10.1016/j.ijimpeng.2021.104057

Zhang ZF, Wang LK, Ming FR, Vadim VS, Chen HL (2017a) Application of smoothed particle hydrodynamics in analysis of shaped-charge jet penetration caused by underwater explosion. Ocean Engineering 145: 177-187. https://doi.org/10.1016/j.oceaneng.2017.08.057

Zhang ZF, Wang LK, Vadim VS (2017b) Damage response of steel plate to underwater explosion: Effect of shaped charge liner. International Journal of Impact Engineering 103: 38-49. https://doi.org/10.1016/j.ijimpeng.2017.01.008

Zhang ZF, Yang SX, Zhang SH, Wang LK, Sui YT, Li T, Zhang GY (2025) Experimental study of damage to double-hull structure by underwater explosions of three charge types-blasting, shaped, and linear shaped charges. International Journal of Impact Engineering 203: 105369. https://doi.org/10.1016/j.ijimpeng.2025.105369